OPTICA

Real-space nanophotonic field manipulation using non-perturbative light–matter coupling

Erika Cortese,[1] Joshua Mornhinweg,[2] Rupert Huber,[2] Christoph Lange,[3] and Simone De Liberato[1,*]

[1]School of Physics and Astronomy, University of Southampton, Southampton, SO17 1BJ, UK
[2]Department of Physics, University of Regensburg, 93040 Regensburg, Germany
[3]Department of Physics, TU Dortmund University, 44227 Dortmund, Germany
*Corresponding author: s.de-liberato@soton.ac.uk

Received 15 August 2022; revised 28 October 2022; accepted 7 November 2022; published 23 December 2022

The achievement of large values of the light–matter coupling in nanoengineered photonic structures can lead to multiple photonic resonances contributing to the final properties of the same hybrid polariton mode. We develop a general theory describing multi-mode light–matter coupling in systems of reduced dimensionality, and we explore their phenomenology, validating our theory's predictions against numerical electromagnetic simulations. On one hand, we characterize the spectral features linked with the multi-mode nature of the polaritons. On the other hand, we show how the interference between different photonic resonances can modify the real-space shape of the electromagnetic field associated with each polariton mode. We argue that the possibility of engineering nanophotonic resonators to maximize multi-mode mixing, and to alter the polariton modes via applied external fields, could allow for the dynamical real-space tailoring of subwavelength electromagnetic fields.

https://doi.org/10.1364/OPTICA.473085

1. INTRODUCTION

Confining light below the Abbe diffraction limit [1] by storing a part of the electromagnetic energy in the kinetic energy of electric charges [2] opened the door to a number of groundbreaking real-world applications, which has contributed to the great success of the field of nanophotonics. In a nanophotonic device, the high energy density of the electromagnetic field makes it relatively easy to couple with different kinds of localized material excitations and reach the strong light–matter coupling regime, originally achieved in cavity quantum electrodynamics (CQED) atomic systems [3]. In such a regime, light and matter degrees of freedom hybridize, leading to novel, polaritonic excitations of a mixed light–matter character [4,5].

Standard theoretical models used to describe strong coupling consider a single optically active matter transition coupled to a single photonic mode. Although some care has to be used when performing calculations on such a reduced Hilbert space [6–9], this single-mode approximation has enabled modeling of a wide range of CQED systems with remarkable easiness and generality. However, the requirement is that the energy spacing between the considered resonances and the neglected ones is much larger than the strength of light–matter coupling, thus permitting to integrate out excited modes with negligible populations.

However, the ongoing race for record coupling strengths [10,11] has led to situations in which higher-energy electronic states cannot be neglected, requiring a model that considers the coupling of multiple matter excitations to the same photonic mode. We refer to this regime as the very-strong coupling (VSC) regime, first predicted by Khurgin in 2001 [12]. The hybridization of multiple excited matter states has an important consequence: the matter component of the polariton, represented itself by a linear superposition of different bare matter wave functions, has a wave function different from each of the bare states [13]. Following a 2013 proposal [14], such an effect was observed for the first time in 2017 [15], as a modification of approximately 30% of the Wannier exciton Bohr radius in GaAs microcavities, and it has been then the object of further theoretical investigations that confirmed the findings [16,17]. Larger numbers of matter states that can be hybridized by coupling with the photonic field could correspond to a broader design space for the resulting electronic wave function. This idea led to the study of systems with a continuum of ionized excitations [18,19] and eventually to the discovery of novel bound excitons stabilized by the photonic interaction [20], and to novel polaritonic loss channels [21].

In this paper, we theoretically investigate the possibility of both multi-mode electronic and multi-mode photonic hybridization, leading to a modification of the spatial electromagnetic profiles of the resulting polariton modes. Given the possibility of fast [22,23] *in situ* tuning of the light–matter interaction by optical and electrical means, subcycle multiwave mixing nonlinearities between different polariton states [24] or even all-optical subcycle switching [25,26], such an approach could open the door to dynamical

manipulation of subwavelength fields, with potential disruptive applications for, e.g., on-chip optical tweezers [27].

Although to the best of our knowledge it was never explicitly discussed in these terms, the regime of photonic VSC has been already described for cold atoms trapped in an optical lattice [28] and reached in various systems, as superconducting qubits coupled to microwave photons in a long transmission-line resonator [29,30]. Moreover, it has been theoretically [31] and experimentally [32] demonstrated in microcavities, where the coupling strength becomes larger than the bare excitation frequencies. In such a regime, the diamagnetic term of the Hamiltonian creates a dominant real-space repulsive interaction localized at the dipole position, which expels the electromagnetic field and may even lead to light–matter decoupling [31,32]. It has also been experimentally observed that, in plasmonic nanocavities, the greatly enhanced coupling between molecular excitons and gap plasmons causes a significant modification of the plasmonic mode profile [33].

Here, we focus on Landau polaritons, where the giant electronic dipoles of cyclotron resonances (CRs) of two-dimensional electron gases (2DEGs) are coupled to strongly enhanced light fields of subwavelength THz resonators. After initial predictions in Ref. [34], multiple experimental realizations followed, some of which established world records for the largest light–matter coupling ever achieved in any CQED system [32,35–37].

In the first part of the paper, we will develop a theory describing multi-mode light–matter strong coupling in CQED. Although the theory is completely general and can be applied to arbitrary polaritonic platforms, for the sake of concreteness, we specialize it to the case of Landau polaritons on which we will test it. Our approach highlights the main electronic and optical features observable for this multi-mode coupling. In the second part, we apply our formalism to structures based on planar plasmonic metasurfaces. To this end, we perform numerical simulations using a commercial finite element method (FEM) software. These simulations verify the predictions of our theory and demonstrate how multi-mode photonic hybridization can lead to a modification of the electromagnetic spatial profile of the polariton modes.

2. THEORY OF MULTI-MODE LIGHT–MATTER COUPLING

In this section, we develop a theory for the light–matter coupling between M photonic resonator modes and the CRs of a 2DEG with a charge carrier density $N_{2\mathrm{DEG}}$ and an effective mass m^*. Following Kohn's theorem [38], we neglect Coulomb interactions between the electrons, which manifest in the nonlinear susceptibility of strongly driven Landau electron systems [39], but have no role in the determination of the optical resonances. Moreover, while our theory technically describes a single quantum well (QW) hosting the entire electron distribution, it is equally valid in densely packed multi-QW structures as usually employed in experiments, where the intensity of the electromagnetic field does not vary significantly within the thickness of the multi-QW stack. Following the elegant theory from Ref. [37], we can write the Hamiltonian of our system as

$$\hat{H} = \hat{H}_{\mathrm{cav}} + \sum_{j=1}^{N} \hbar\omega_c \hat{c}_j^{\dagger}\hat{c}_j + \frac{e^2}{m^*}\sum_{j=1}^{N} \hat{A}_-(\mathbf{r}_j)\hat{A}_+(\mathbf{r}_j) + i\sqrt{\frac{\hbar\omega_c e^2}{m^*}}\sum_{j=1}^{N}\left[\hat{c}_j^{\dagger}\hat{A}_+(\mathbf{r}_j) - \hat{c}_j\hat{A}_-(\mathbf{r}_j)\right], \tag{1}$$

where $\hat{c}_j$ is the Bosonic lowering operator for the electrons, leading to a transition from the jth to the $(j-1)$th Landau level with a transition energy $\hbar\omega_c$, and $\hat{H}_{\mathrm{cav}}$ is the Hamiltonian describing the bare electromagnetic field in the resonator. In case of high electron density and strong in-plane confinement of both the 2DEG and the electromagnetic field, plasmonic modes hosted by the system can be nonnegligible and lead to the formation of magneto-plasmon modes with a renormalized frequency of $\tilde{\omega}_c = \sqrt{\omega_c^2 + \omega_P^2}$, where ω_P is the 2D plasmon frequency for the 2DEG [21]. However, a correct estimation of ω_P not only takes into account the in-plane confinement of the 2DEG, but also includes the screening of the metallic resonator in proximity of the electrons, leading to a reduction of the plasmon energy [40–42]. For our structures, this effect strongly limits the extent of renormalization such that we disregard plasmon effects.

In Eq. (1), we introduced the non-Hermitian vector potentials written in terms of the in-plane component of the vector potential $\hat{\mathbf{A}}(\mathbf{r})$ as

$$\hat{A}_{\pm}(\mathbf{r}) = \frac{\hat{A}_x(\mathbf{r}) \mp i\hat{A}_y(\mathbf{r})}{\sqrt{2}}. \tag{2}$$

The full vector potential can be expressed as a sum of photonic modes with dimensionless spatial field profiles $\mathbf{f}_\nu(\mathbf{r})$, frequencies ω_ν, and second-quantized bosonic annihilation operators $\hat{a}_\nu$ as

$$\hat{\mathbf{A}}(\mathbf{r}) = \sum_\nu \sqrt{\frac{\hbar}{2\epsilon_0\epsilon_r(\mathbf{r})\omega_\nu\mathcal{V}_\nu}}\mathbf{f}_\nu(\mathbf{r})\left(\hat{a}_\nu^{\dagger} + \hat{a}_\nu\right). \tag{3}$$

Here, the vector fields $\mathbf{f}_\nu(\mathbf{r})$ are eigensolutions of Maxwell's equations for the bare cavity, and they are thus orthogonal over the full domain $\mathbb{V}$ [43]:

$$\int_{\mathbb{V}} \mathbf{f}_\nu^*(\mathbf{r})\mathbf{f}_\mu(\mathbf{r})\mathrm{d}\mathbf{r} = \mathcal{V}_\nu\delta_{\nu,\mu}, \tag{4}$$

with $\mathcal{V}_\nu$ the mode volume of the νth photon mode and $\epsilon_r(\mathbf{r})$ the background, non-resonant dielectric constant. The amplitudes of the non-Hermitian vector potentials then take the form

$$\hat{A}_-(\mathbf{r}) = \sum_\nu \sqrt{\frac{\hbar}{2\epsilon_0\epsilon_r(\mathbf{r})\omega_\nu\mathcal{V}_\nu}} f_\nu(\mathbf{r})\left(\hat{a}_\nu^{\dagger} + \hat{a}_\nu\right),$$

$$\hat{A}_+(\mathbf{r}) = \sum_\nu \sqrt{\frac{\hbar}{2\epsilon_0\epsilon_r(\mathbf{r})\omega_\nu\mathcal{V}_\nu}} f_\nu^*(\mathbf{r})\left(\hat{a}_\nu^{\dagger} + \hat{a}_\nu\right), \tag{5}$$

with

$$f_\nu(\mathbf{r}) = \frac{f_{\nu,x}(\mathbf{r}) + i f_{\nu,y}(\mathbf{r})}{\sqrt{2}}. \tag{6}$$

Crucially, the orthogonality condition in Eq. (4) holds only if the integral is performed over the entire three-dimensional space, while the integral of two orthogonal modes over any sub-domain does not vanish in general. This concept is illustrated in Fig. 1 for the model case of a planar microcavity (a), (b) and for a split-ring resonator (c), (d), integrated over either the full three-dimensional volume (a), (c) or a thin, quasi-two-dimensional surface (b), (d). In both cases, two orthogonal modes (red and blue arrows) become non-orthogonal when the integral is performed over a quasi-two-dimensional slice of the overall volume. To understand how this

finding is relevant for our systems, we can consider as an example the third term of Eq. (1), the so-called diamagnetic term of the light–matter interaction Hamiltonian, which contains generally non-vanishing expressions of the form

$$\sum_{j=1}^{N} f_\nu^*(\mathbf{r}_j) f_\mu(\mathbf{r}_j) = N_{2\mathrm{DEG}} \int_{\mathbb{S}} f_\nu^*(z, \mathbf{r}_\parallel) f_\mu(z, \mathbf{r}_\parallel) \mathrm{d}\mathbf{r}_\parallel, \tag{7}$$

where $\mathbb{S}$ is the sample surface, z is the out-of-plane position of the 2DEG, and $\mathbf{r}_\parallel$ is the in-plane position. Placing a 2DEG at the center of the planar microcavity, or below the split-ring resonator, will thus result in an interaction of different photon modes that is mediated and modulated by the coupling to the electrons. We now elucidate this insight further, showing how it is relevant also for the dipolar light–matter interaction described by the fourth term of Eq. (1). To this aim, let us call M the number of photonic modes in the frequency region of interest. Their wave functions, restricted over the sample surface $\mathbb{S}$, span a space of dimension at most M. We can thus always introduce M orthonormal basis functions over $\mathbb{S}$,

$$\int_{\mathbb{S}} \phi_\nu^*(\mathbf{r}_\parallel) \phi_\mu(\mathbf{r}_\parallel) \mathrm{d}\mathbf{r}_\parallel = \delta_{\nu,\mu}, \tag{8}$$

such that

$$f_\nu(z, \mathbf{r}_\parallel) = \sum_{\mu \le \nu} \alpha_{\nu,\mu} \phi_\mu(\mathbf{r}_\parallel). \tag{9}$$

It is always possible to choose the basis such that $\alpha_{1,1}$ is real and $\alpha_{\nu,\mu} = 0$ if $\nu < \mu$. Using Eq. (9), the degree of non-orthogonality between the resonator modes with respect to the QW plane can be captured by defining the overlap matrix

$$\mathcal{F}_{\nu,\mu} = \int_{\mathbb{S}} f_\nu^*(z, \mathbf{r}_\parallel) f_\mu(z, \mathbf{r}_\parallel) \mathrm{d}\mathbf{r}_\parallel = \sum_{\gamma \le \min(\nu,\mu)} \alpha_{\nu,\gamma}^* \alpha_{\mu,\gamma}, \tag{10}$$

and its normalized version

$$\eta_{\nu,\mu} = \frac{\mathcal{F}_{\nu,\mu}}{\sqrt{\mathcal{F}_{\mu,\mu}\mathcal{F}_{\nu,\nu}}}, \tag{11}$$

both of which may assume values from zero to one. These matrices quantify the spatial overlap of any pair (μ, ν) of photon modes over the QW plane. A diagonal matrix $\eta_{\nu,\mu} \propto \delta_{\nu,\mu}$ implies vanishing overlap between the photon modes, while a fully populated matrix corresponds to a strong overlap.

By introducing a set of collective Bosonic matter operators,

$$\hat{b}_\mu = \frac{1}{\sqrt{N_{2\mathrm{DEG}}}} \sum_{j=1}^{N} \phi_\mu(\mathbf{r}_{j,\parallel}) \hat{c}_j, \tag{12}$$

with the in-plane position $\mathbf{r}_{j,\parallel}$ of the jth electron, we can finally write the Hamiltonian in Coulomb gauge as

$$\begin{aligned} \hat{H} = & \sum_\nu \hbar\omega_\nu \hat{a}_\nu^\dagger \hat{a}_\nu + \sum_\nu \hbar\omega_c \hat{b}_\nu^\dagger \hat{b}_\nu \\ & + \sum_{\nu,\mu} h_{\nu,\mu} \left(\hat{a}_\nu^\dagger + \hat{a}_\nu\right)\left(\hat{a}_\mu^\dagger + \hat{a}_\mu\right) \\ & + \sum_\nu \sum_{\mu \le \nu} \left[\left(g_{\nu,\mu} \hat{b}_\mu + g_{\nu,\mu}^* \hat{b}_\mu^\dagger\right)\left(\hat{a}_\nu^\dagger + \hat{a}_\nu\right)\right]. \end{aligned} \tag{13}$$

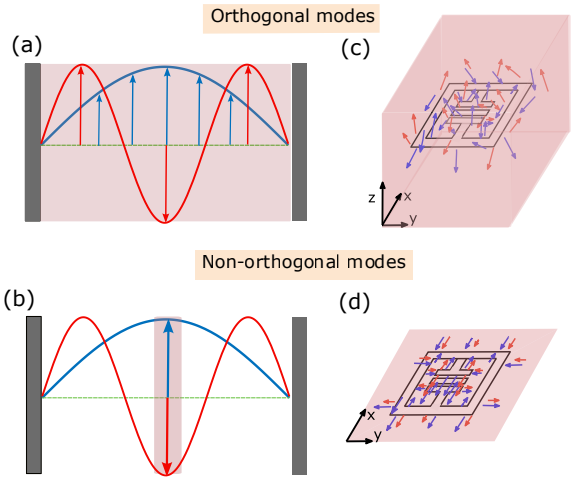

Fig. 1. Sketch of how orthogonal resonator modes can become non-orthogonal when coupled over an active region occupying only part of the resonator volume. Shown are the case of a planar microcavity (a), (b) and a split-ring resonator (c), (d). Two electromagnetic modes are shown by red and blue arrows, and the active region, corresponding to the full three-dimensional volume (a), (c) or a thin, quasi-two-dimensional surface (b), (d), is shaded in light red.

Here,

$$g_{\nu,\mu} = \alpha_{\nu,\mu} \sqrt{\frac{\hbar^2 \omega_c N_{2\mathrm{DEG}} e^2}{2m^* \epsilon_0 \bar{\epsilon}_r \omega_\nu \mathcal{V}_\nu}},$$

$$h_{\nu,\mu} = \sum_{\gamma \le \nu,\mu} \frac{g_{\nu,\gamma} g_{\mu,\gamma}}{\hbar\omega_c} \tag{14}$$

represent coupling parameters, $g_{\nu,\mu}$ is the vacuum Rabi energy quantifying the coupling between the photonic mode ν and the matter mode μ, while $h_{\nu,\mu}$ quantifies the diamagnetic coupling between two photonic modes mediated by the matter. In Eq. (14), we also introduced the background dielectric constant of the QW material $\bar{\epsilon}_r$. This Hamiltonian is bosonic and quadratic, which allows us to determine its eigenmodes by Hopfield diagonalization [44]. Moreover, it presents some important features. First, the light–matter interaction term displays cross-interactions between different spatial modes, in both the diamagnetic term [second line of Eq. (13)] and in the light–matter coupling term [third line of Eq. (13)]. Second, it presents so-called antiresonant terms, products of two creation or two annihilation operators. Those terms, which cannot be intuitively interpreted as describing excitation exchanges between different fields, become important in the ultrastrong coupling regime [10,11]. They cannot be neglected when the vacuum Rabi energy becomes comparable to the energies of the bare light and matter modes, with a ratio of 0.1 being usually considered the threshold to enter the ultrastrong coupling regime. Starting from such a value, the antiresonant terms have in fact led to measurable shifts in the polaritonic frequencies [45] as well as to more exotic phenomenology, as the presence of a nonnegligible population of virtual excitations in the ground state [46].

Following the Hopfield approach, we diagonalize the Hamiltonian by introducing the hybrid multi-mode polariton operators

$$\hat{p}_\mu = \sum_\nu \left(x_{\nu,\mu} \hat{a}_\nu + w_{\nu,\mu} \hat{b}_\nu + y_{\nu,\mu} \hat{a}_\nu^\dagger + z_{\nu,\mu} \hat{b}_\nu^\dagger\right), \tag{15}$$

whereby $(x_{\nu,\mu}, w_{\nu,\mu}, y_{\nu,\mu}, z_{\nu,\mu})$ are real-valued Hopfield coefficients. The dressed polariton frequencies ω_μ^p are the eigenvalues of the polariton eigenequation

$$\hbar\omega_\mu^p \hat{p}_\mu = \left[\hat{p}_\mu, \hat{H}\right]. \tag{16}$$

The Hopfield transformation can subsequently be inverted as

$$\left(\hat{a}_\nu + \hat{a}_\nu^\dagger\right) = \sum_\mu (x_{\nu,\mu} - y_{\nu,\mu})\left(\hat{p}_\mu + \hat{p}_\mu^\dagger\right), \tag{17}$$

allowing us to find the coupled electric field components corresponding to the non-Hermitian vector potential:

$$\hat{E}_-(\mathbf{r}) = \sum_{\nu,\mu} \sqrt{\frac{\hbar\omega_\nu}{2\epsilon_0\bar{\epsilon}_r\mathcal{V}_\nu}} f_\nu(\mathbf{r})(x_{\nu,\mu} - y_{\nu,\mu})\left(\hat{p}_\mu^\dagger + \hat{p}_\mu\right),$$

$$\hat{E}_+(\mathbf{r}) = \sum_{\nu,\mu} \sqrt{\frac{\hbar\omega_\nu}{2\epsilon_0\bar{\epsilon}_r\mathcal{V}_\nu}} f_\nu^*(\mathbf{r})(x_{\nu,\mu} - y_{\nu,\mu})\left(\hat{p}_\mu^\dagger + \hat{p}_\mu\right). \tag{18}$$

From Eq. (18), we can clearly see that, as expected from our initial discussion, the electric field corresponding to the polaritonic mode $\hat{p}_\mu$ is a linear combination of all bare electromagnetic mode profiles $f_\nu(\mathbf{r})$, each weighted by the Hopfield coefficients. When the vacuum Rabi energies in Eq. (14) become comparable to the energy spacing between different resonator modes, multiple terms of such a linear combination can become nonnegligible. In this case, the interference of different bare electromagnetic modes weighed by the relative Hopfield coefficients can strongly modify the spatial profile of the polariton electromagnetic mode, the hallmark of photonic VSC described in the Introduction.

We stress that we have developed an inherently lossless theory based on a system Hamiltonian. This model is justified because we deal with systems in which we can identify discrete, albeit broadened, independently addressable electromagnetic modes. The VSC physics is due to the interaction between the optically active material and these intra-cavity modes. Losses then cause only a Lorentzian broadening, which can be taken into account *a posteriori* using one of the perturbative schemes that have been devised for systems in the ultrastrong coupling regime [47,48], without affecting the VSC phenomenology object of this paper. This is proven by the fact our lossless theory fits well the numerical FEM results, even if the highest photonic mode is substantially broadened. A finite linewidth can be understood as a frequency uncertainty, which translates in an uncertainty of the same order on the value of the cyclotron frequency corresponding to a specific interference figure. For such a reason, when comparing snapshots of field profiles between the lossless Hamiltonian theory and lossy FEM results, we will fit the cyclotron frequency within half of the resonance linewidth.

The opposite case, VSC with a continuum, has been achieved, both the standard electronic version [20] and the photonic one [30], and multiple approaches have been developed to study the coupling with a photonic continuum in the ultrastrong coupling regime [19,46]. These are nevertheless not relevant for the system considered here but rather a topic for future investigations.

Note moreover that systems with structured photonic continua can be described as multiple interacting resonances [49,50]. However, this is unrelated to the VSC effect we study here, as in such a case, the interaction is a weak coupling effect between spectrally overlapping modes, independent of the coupling with optically active material.

3. SEMI-ANALYTICAL RESULTS

To highlight the role of the normalized overlap factors for the coupling strength, we now assume a single pair of photonic modes ($M = 2$) with frequencies ω_1 and ω_2 and mode volumes $\mathcal{V}_1$ and $\mathcal{V}_2$. Their non-orthogonality is quantified by a single overlap parameter $\eta_{2,1}$. By expliciting Eq. (10), we arrive at

$$\begin{aligned}\mathcal{F}_{1,1} &= \alpha_{1,1}^2,\\ \mathcal{F}_{2,2} &= |\alpha_{2,1}|^2 + |\alpha_{2,2}|^2,\\ \mathcal{F}_{2,1} &= \alpha_{2,1}^*\alpha_{1,1},\end{aligned} \tag{19}$$

which leads to

$$\begin{aligned}\alpha_{1,1} &= \sqrt{\mathcal{F}_{1,1}},\\ \alpha_{2,1} &= \frac{\mathcal{F}_{2,1}^*}{\sqrt{\mathcal{F}_{1,1}}} = \sqrt{\mathcal{F}_{2,2}}\eta_{2,1}^*,\\ \alpha_{2,2} &= \sqrt{\mathcal{F}_{2,2} - \frac{|\mathcal{F}_{2,1}|^2}{\mathcal{F}_{1,1}}} = \sqrt{\mathcal{F}_{2,2}}\sqrt{1 - |\eta_{2,1}|^2}.\end{aligned} \tag{20}$$

Defining the renormalized mode volume as $\tilde{\mathcal{V}}_\nu = \frac{\mathcal{V}_\nu}{\mathcal{F}_{\nu,\nu}}$, Eq. (14) leads to expressions for the coupling strengths:

$$\begin{aligned}g_{1,1} &= \sqrt{\frac{\hbar^2\omega_c N_{2\mathrm{DEG}} e^2}{2m^*\epsilon_0\bar{\epsilon}_r\omega_1\tilde{\mathcal{V}}_1}},\\ g_{2,1} &= \sqrt{\frac{\hbar^2\omega_c N_{2\mathrm{DEG}} e^2}{2m^*\epsilon_0\bar{\epsilon}_r\omega_2\tilde{\mathcal{V}}_2}}\eta_{2,1},\\ g_{2,2} &= \sqrt{\frac{\hbar^2\omega_c N_{2\mathrm{DEG}} e^2}{2m^*\epsilon_0\bar{\epsilon}_r\omega_2\tilde{\mathcal{V}}_2}}\sqrt{1 - |\eta_{2,1}|^2}.\end{aligned} \tag{21}$$

For the given basis, the interpretation of these coefficients is that the photonic mode $\nu = 1$ is coupled to only a single matter mode, $\mu = 1$. In contrast, the coupling strength for the photonic mode $\nu = 2$ originates from simultaneous coupling to both matter modes owing to the non-vanishing overlap parameter $\eta_{2,1}$.

To show the peculiar spectroscopic features expected in systems with nonnegligible overlap between the photonic modes, we plot in Fig. 2 the spectra obtained by diagonalizing the Hamiltonian in Eq. (13) for two resonator modes. The three cases concern settings of vanishing overlap [$\eta_{2,1} = 0$; (a), (b)], medium overlap [$\eta_{2,1} = 0.5$; (c), (d)], and maximum overlap [$\eta_{2,1} = 1$; (e), (f)], whereby in each case, the left and right panels show spectra as a function of the cyclotron frequency and electron density $N_{2\mathrm{DEG}}$, respectively.

We can point out two characteristic signatures for the overlap. First, we consider varying the cyclotron frequency [(a), (c), (e)]. For vanishing mode overlap $\eta_{2,1} = 0$ [(a)], we observe the opening of separate polariton gaps for each pair of photonic mode and matter excitation. On the contrary, maximum overlap of $\eta_{2,1} = 1$ [(e)] leads to the emergence of an S-shaped resonance (blue curve). In this case, the mode structure originates from the coupling of a

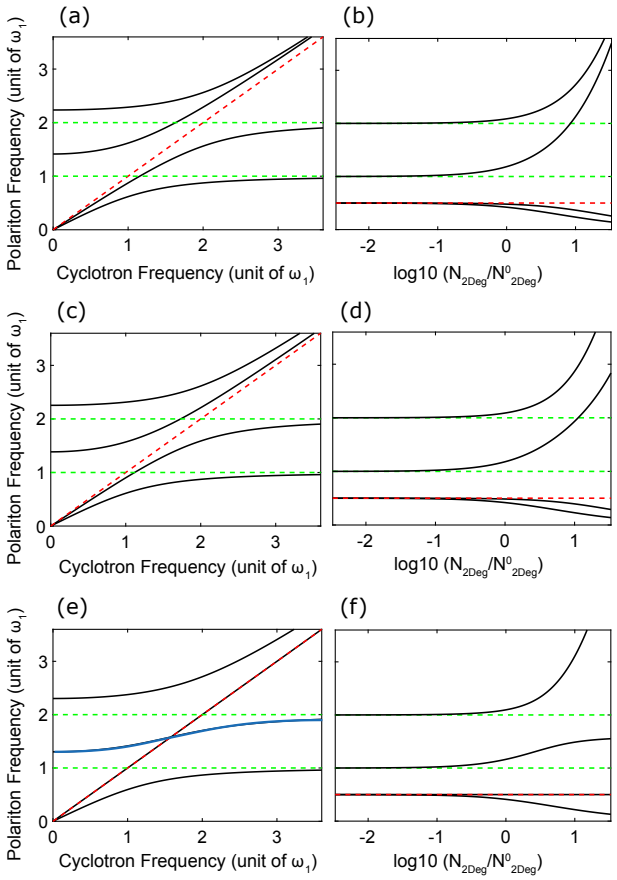

Fig. 2. Polaritonic eigenmodes arising from the diagonalization of Eq. (13) with $M = 2$ photonic resonances of frequencies ω_1 and $\omega_2 = 2\omega_1$ (green dashed lines) coupled to the 2DEG hosting the cyclotron resonance, ω_c (red dashed line). The three rows correspond to the case of zero overlap between the two photonic modes [$\eta_{2,1} = 0$; (a), (b)], medium overlap [$\eta_{2,1} = 0.5$; (c), (d)], or perfect overlap [$\eta_{2,1} = 1$; (e), (f)]. Panels in the left column (a), (c), (e) are shown as a function of the cyclotron frequency ω_c with resonant couplings in the zero overlap case ($\eta_{2,1} = 0$) $g_{1,1} = 0.5\hbar\omega_1$ at $\omega_c = \omega_1$ and $g_{2,2} = 0.25\hbar\omega_2$ at $\omega_c = \omega_2$. Panels in the right column (b), (d), (f) are shown for a fixed value of the cyclotron frequency $\omega_c = 0.5\omega_1$ as a function of the electron density $N_{2\mathrm{DEG}}$. The reference density $N^0_{2\mathrm{DEG}}$ corresponds to resonant couplings in the left column. Panel (e) displays an S-shaped polariton curve (blue solid line) due to a perfect overlap.

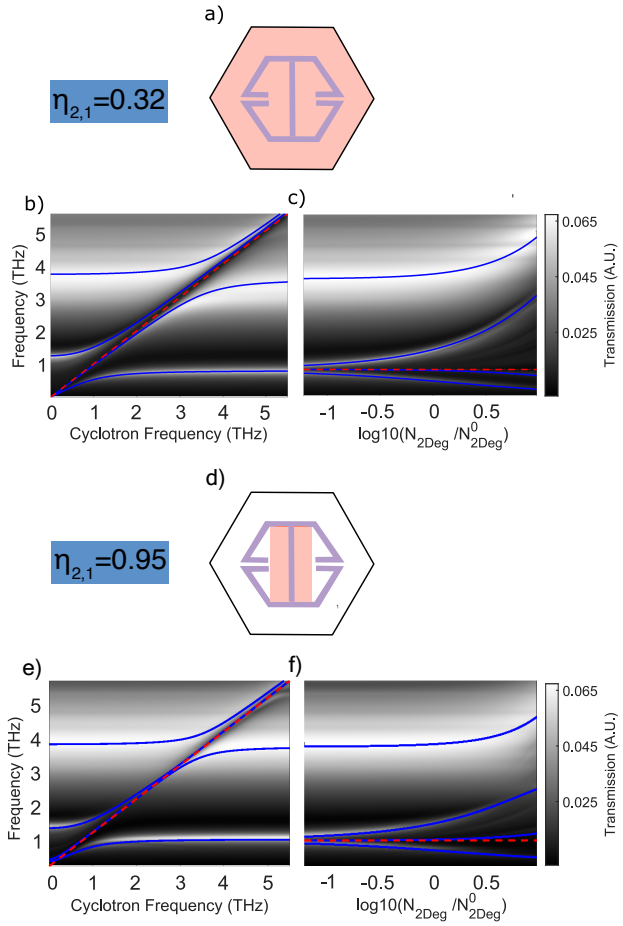

Fig. 3. Sketch of the structure including the hexagonal negative THz resonator (violet shape) fabricated on top of the GaAs substrate (white region), and the QW hosting the 2DEG (light red region), whose area occupies either the whole unit cell (a) or a limited area enclosing the central gap (d). In the other panels, we show numerical calculations of the transmission as a function of cyclotron frequency ω_c at a fixed electron density $N^0_{2\mathrm{DEG}} = 3 \times 10^{12}\ \mathrm{cm}^{-2}$ (b), (f) and as a function of electron density at a fixed cyclotron frequency $\omega_c = 0.8$ THz (c), (g). Panels (b), (c) illustrate results for the structure in panel (a), and panels (f), (g) for the structure in panel (e). The calculated values of $\eta_{2,1}$ are shown in (a), (d). Blue solid lines highlight the fitted polaritonic resonances.

single matter excitation $\mu = 1$ to both photonic modes $\nu = 1, 2$, simultaneously, leading to three polariton branches in total. The S-shaped center mode is confined between the cavity frequencies ω_1 and ω_2, thus manifesting a double-mode nature. Second, we analyze the mode structure as a function of electron density [(b), (d), (f)]. Here, we see that at larger densities and thus larger couplings, two modes blueshift in the case of vanishing overlap, while a single mode blueshifts in the presence of substantial overlap. We attribute this behavior to the contribution of the diamagnetic term, which, being of higher order in $N_{2\mathrm{DEG}}$, becomes dominant at very large densities and tends to blueshift the upper polariton of each set of polaritonic solutions, taking into account that polaritonic modes never cross their bare components [31,51]. Nevertheless, in the case of maximum overlap, the diamagnetic term between the two photonic modes leads to a repulsion of the upper polaritons, leading to an anti-crossing behavior above a certain critical value of the electronic density.

4. NUMERICAL RESULTS

To explore the relevance of our theory for experiments with Landau polaritons, we used a commercial FEM software to compute the complex field distribution and transmission spectra without any fitting parameter.

Our structure is a *negative* resonator (cut from a gold surface, Fig. 3) [52] of hexagonal shape, fabricated on top of a gallium arsenide (GaAs) substrate [white areas in Figs. 3(a) and 3(d)], with the CRs hosted in three GaAs QWs, each doped at a density $N_{2\mathrm{DEG}}/3$ [light red regions in Figs. 3(a) and 3(d)], so that the total surface carrier density is $N_{2\mathrm{DEG}}$. The approach we used to simulate the metamaterial coupled to the doped multiple QW stack was reported by Bayer *et al.* [32], and we will briefly resume the main steps below.

To reduce the numerical complexity of modeling the dielectric environment composed of several QWs and corresponding barriers, we employ an effective medium approach describing the full QW stack as a layer of a total thickness of $d_{\mathrm{QW}} = 210$ nm and total

surface density N_{2DEG} [53]. The CR of the 2DEG is implemented as a gyrotropic medium, where the dielectric tensor of a plasma of charge carriers magnetically biased along the z direction describes the two-dimensional polarization response of the CR in the plane perpendicular to the magnetic field:

$$\epsilon_{CR} = \begin{pmatrix} \epsilon_{xx}(\omega) & i\epsilon_{xy}(\omega) & 0 \\ -i\epsilon_{xy}(\omega) & \epsilon_{xx}(\omega) & 0 \\ 0 & 0 & \bar{\epsilon}_r \end{pmatrix}, \tag{22}$$

with

$$\epsilon_{xx}(\omega) = \bar{\epsilon}_r - \frac{\omega_{P3D}^2(\omega + i\Gamma)}{\omega\left[(\omega + i\Gamma)^2 - \omega_c^2\right]},$$

$$\epsilon_{xy}(\omega) = \frac{\omega_{P3D}^2\omega_c}{\omega\left[(\omega + i\Gamma)^2 - \omega_c^2\right]}. \tag{23}$$

Here, ω_{P3D} is the characteristic plasma frequency describing the oscillation of the electrons with a homogeneous 3D density N_{2DEG}/d_{QW}, and Γ is the phenomenological scattering rate. In the z direction, we employ only the background dielectric constant, as the confinement inhibits a plasma response. For the gold metamaterial, we use the dielectric constant $\epsilon_{Au} = 10^5 + 10^5 i$ [32] to approximate the response of a perfect metal. In the $x - y$ direction, we employ periodic boundary conditions to reflect the array character of our structure. Maxwell's equations are subsequently solved numerically. The transmission is derived from the electric field amplitude calculated in the far field and is expected to predict the experimental results across the entire spectral range with high accuracy.

To explore the direct impact of the overlap over the optical spectrum, we consider two types of QW designs. In the first layout, the 2DEG covers the whole unit cell area [Fig. 3(a)]. We refer to this design as *unstructured*. A second layout is instead realized by in-plane confinement of the 2DEG within a small rectangular patch at the center of the resonator [Fig. 3(d)]. We refer to this layout as *structured*.

The numerical transmissions for the four samples are shown in Figs. 3(b) and 3(e) as a function of the cyclotron frequency, and in Figs. 3(c) and 3(f) as a function of the electron density N_{2DEG}. The simulation is performed considering an exciting electromagnetic wave that is linearly polarized along the gap (x) direction, and incident perpendicularly to the metamaterial plane. From the transmission spectrum at low electronic density, shown in Fig. 4(a), we recognize $M = 2$ active photon resonances within the given frequency range, whose in-plane field profiles along the gap direction are plotted in Figs. 4(b) and 4(c).

In the structured case, the patch acts as a Fabry–Perot resonator for the quasi-2D plasmonic excitations of the electron gas in the QWs [54]. This leads to a non-vanishing frequency for the fundamental plasmonic mode to which the lower polariton in Fig. 3(e) would converge for a vanishing cyclotron frequency. We estimated the fundamental plasmon mode frequency using the formula [40]

$$\omega_P{}^0 = \sqrt{\frac{N_{2DEG}e^2\pi}{2m^*\epsilon_0\epsilon_{eff}W}}, \tag{24}$$

with W the patch width and ϵ_{eff} the effective permittivity taking into account the screening of the gold resonator by averaging the screened and unscreened portions of the QW area. The resulting

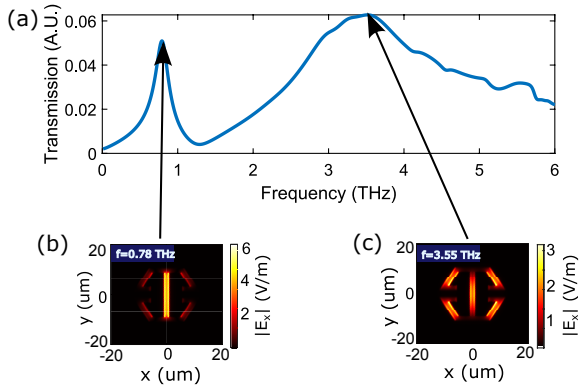

Fig. 4. Transmission spectra for the resonator (a). The resonances with frequencies up to 5 THz are identified by black arrows, and the corresponding in-plane field distribution along the gap direction is plotted for each of the $M = 2$ resonances in (a) with bare frequencies $\omega_1 = 0.78$ THz (b) and $\omega_2 = 3.55$ THz (c).

value is $\omega_P{}^0 \approx 0.2$ THz. Although for the sake of completeness, we did use such a value in our simulations for the structured QWs, we notice that for such low frequencies, the polaritons have vanishing photonic components and the transmission spectra are not noticeably affected by the exact value of ω_p^0.

Once we calculated the overlap parameter as in Eq. (11) for the two configurations, we employed our multi-mode theory to fit simultaneously the resonances for the spectra of both the ω_c-sweep and the N_{2DEG}-sweep, considering the matter resonance as the magnetoplasmon mode $\tilde{\omega}_c$ and treating the normalized mode volumes $\tilde{\mathcal{V}}_v$ as fitting parameters.

From the discussion in the previous section, we expect that passing from the unstructured to the structured sample, as the integration surface is reduced, not only the normalized mode volumes $\tilde{\mathcal{V}}_v$ will vary, but also the modes will become less orthogonal, thus increasing the overlap parameter $\eta_{2,1}$. This is indeed the case as can be seen by the calculated values of $\eta_{2,1} = 0.32$ for the unstructured sample in Fig. 3(a) and of $\eta_{2,1} = 0.95$ for the structured sample in Fig. 3(d) derived by Eq. (11).

Comparing the transmission spectra for the different configurations allows us to recognize, albeit in attenuated form, the main differences in the spectral features predicted by the theory (marked on the plots by blue solid lines). At first glance, we notice that the single polariton anti-crossings are well resolved in the unstructured case, as they mainly arise from one-to-one coupling of photonic modes to orthogonal matter excitations. In the structured platform instead, we observe a reduction of the polariton splitting, and the appearance of an S-shaped resonance. The reduction of the polariton splitting is mainly due to the fact that reducing the integration area for the single mode leads to a larger normalized mode volume $\tilde{\mathcal{V}}_v$, and as such to a smaller coupling strength. On the other hand, the confinement of the 2DEG around the central gap of the resonator increases the overlap between modes, which becomes close to one, leading to the appearance of the characteristic S-shaped polariton.

We report in Fig. 5 the in-plane electric field distributions along the gap direction for the coupled modes of the hexagonal resonator platform in the structured configuration. The reported data sets are extracted from the FEM simulation and calculated by our multi-mode theory, and are plotted on the right and left sides of (a)–(e). The simulation field maps for a given coupled mode are

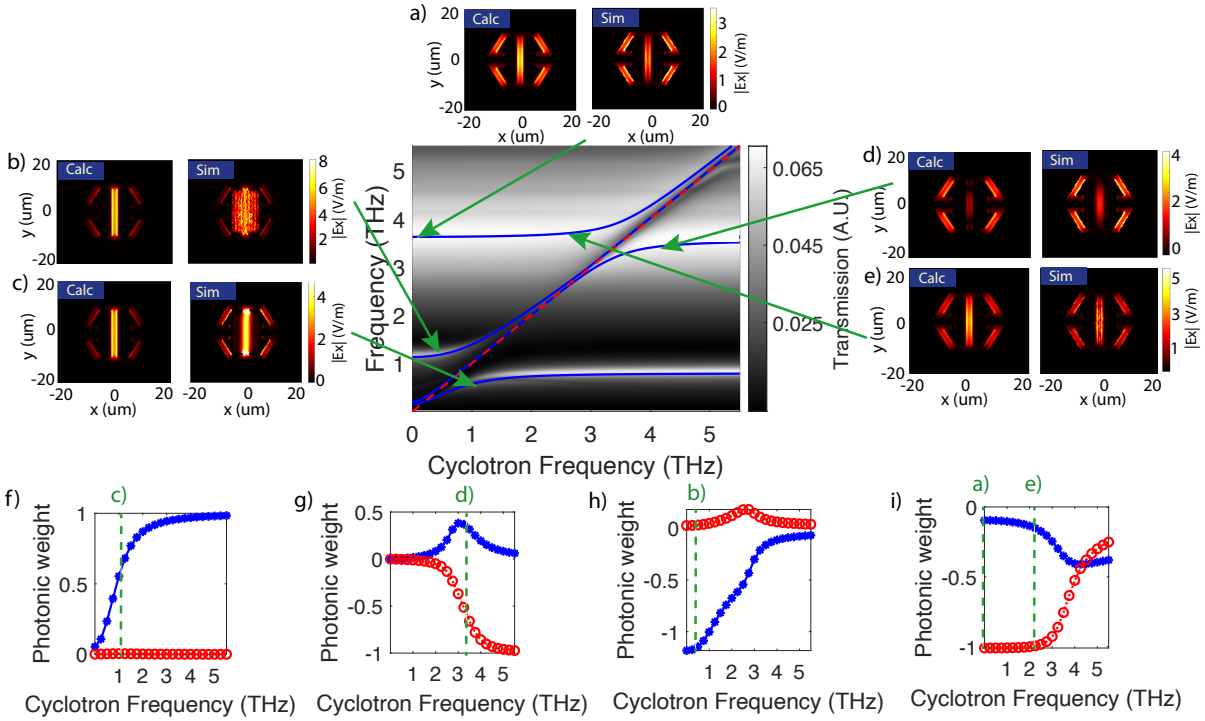

Fig. 5. Simulated transmission spectrum as function of ω_c at $N_{2\mathrm{DEG}} = 3 \times 10^{12}\mathrm{cm}^{-2}$ for the hexagonal resonator shown in Fig. 3(d), corresponding to the overlap factor $\eta_{2,1} = 0.95$. The colormaps (a)–(e) represent the in-plane electric field profile along the gap direction $|E_x|$ (y-component results negligible), extracted on the QW plane, corresponding to the coordinates marked by the green arrows. The bottom panels (f)–(i) display the weight $|x_{\nu,\mu} - y_{\nu,\mu}|$ of the photonic mode ν in the polariton mode μ, as appearing in Eq. (18) for all polariton modes, with the coordinates of the colormaps above marked by dashed green lines. The (f)–(i) plots are ordered following an ascendant order for the polariton frequencies.

obtained by simulating the far-field excitation of the system at the specific value of ω_c, marked by the green arrows in the ω_c-sweep transmission plot, with excitation frequency corresponding to that of the polariton mode.

The corresponding theoretical electric field profiles are instead obtained by Eq. (18) as linear combinations of the numerically extracted fields of the uncoupled resonances, shown in Fig. 4, weighed by the photonic coefficients displayed in Figs. 5(f)–5(i). Note that, as explained at the end of Section 2, the linear superposition is calculated at a cyclotron frequency fitted within half of the resonance linewidth from the nominal one. By observing the field maps, we can notice that these refer to three different cases: Figs. 5(a), (c), and (e) display field distributions similar to the uncoupled ones, as the weight of one of the two modes is greatly dominant over the other. Figure 5(d) displays a case in which the two photonic weights are comparable, and the electric field map is noticeably different from either of the bare ones. Finally, in Fig. 5(b), our theory predicts the field of the bare photonic mode mainly localized in the central gap, while the simulation shows the electric field diffracting in the far field of the plasma waves, although remaining confined on the area of the QW patch. This effect is related to the one recently investigated in Ref. [21]. Here, the authors point out how the electromagnetic field, confined in the resonator gap, can excite a continuum of propagative high-wave-vector plasmonic waves leaking away energy from the polaritonic resonances. In our case, the main difference is that the patch acts as a Fabry–Perot resonator. Even if higher-order discrete modes are quasi-resonant with one more polaritonic branch, the energy of the excited modes remains confined in the patch and has thus only a limited effect on the polaritonic resonances [55]. Our two-mode Hopfield model misses this effect, which could nevertheless be correctly described expanding the basis to include many discrete plasmonic modes of the patch [18] or alternatively using a theory able to deal with continuum spectra [19].

Finally, Fig. 6 highlights the modification of the in-plane electric field driven by the multi-mode hybridization for the specific case of the second polariton mode across the anti-crossing point with the higher photonic frequency $\omega_2 = 3.55$ THz. The calculated electric field maps in (c) refer to the cyclotron frequency values marked by the vertical black dashed lines in (a) and (b) [same as Fig. 5(g)]. We can clearly see how changing the cyclotron frequency varies the electric field map, displacing the minimum of the field across the subwavelength central gap, a feature suggestive of potential applications in subwavelength sensing and optical tweezers.

Our results thus demonstrate that, by optimizing the resonator-2DEG structure, we are able to dynamically modify the subwavelength electromagnetic field profile, moving its maxima by varying the applied magnetic field.

5. CONCLUSION

In conclusion, we theoretically investigated the multi-mode coupling between the CRs of a 2DEG and highly confined THz-resonator modes. We developed a general theory describing multi-mode coupling taking into account the non-orthogonality of the electromagnetic modes. We highlighted specific spectral features due to the presence of multiple photonic modes and demonstrated the possibility to tune the level of inter-mode coupling by lateral confinement of the 2DEG. Finally, using these

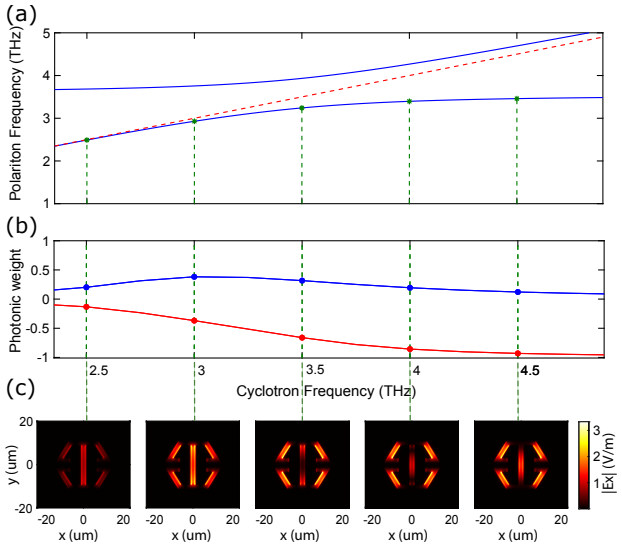

Fig. 6. Evolution of the electric field map for the second lower polariton mode. (a) Frequency dispersion for the second and fourth coupled modes (blue solid lines) as a function of the cyclotron frequency (red dashed line) at the fixed electron density $N_{2DEG} = 3 \times 10^{12}$ cm^{-2}. (b) Photonic weight components ($\nu = 1$ blue dotted curve, $\nu = 2$ red dotted curve) for the second (lower) polariton mode. (c) In-plane electric field profiles corresponding to the frequency coordinates marked by the vertical green dashed lines in (a) and (b).

effects opens up the possibility to dynamically tailor the spatial profile of subwavelength electromagnetic modes by varying the applied static magnetic field. This approach can potentially be used to realize subwavelength optical tweezers to trap and move nanoparticles over sub-micrometer distances.

The theoretical results encourage us to explore novel experimental methods and setups allowing to observe the predicted modification of the electric field profiles, driven by the coupling. Moreover, we aim to investigate further different resonator configurations to maximize the effects of multi-mode hybridization, heading towards novel quantum technological applications, based on a controllable and potentially dynamical tuning of highly confined electromagnetic fields.

Funding. Deutsche Forschungsgemeinschaft (DFG) (LA 3307/1-2); Royal Society (RGF\EA\181001); Leverhulme Trust (RPG-2022-477 037, Philip Leverhulme Prize).

Acknowledgment. S.D.L. is a Royal Society Research Fellow. S.D.L. and E.C. acknowledge funding by the Leverhulme Trust and the Royal Society. C.L. and J.M. acknowledge funding by the DFG.

Disclosures. The authors declare no conflicts of interest.

Data availability. The data that support the findings of this study are available from the corresponding authors on reasonable request.

REFERENCES

1. D. Ballarini and S. De Liberato, "Polaritonics: from microcavities to sub-wavelength confinement," Nanophotonics **8**, 641–654 (2019).
2. J. B. Khurgin, "Relative merits of phononics vs. plasmonics: the energy balance approach," Nanophotonics **7**, 305–316 (2018).
3. S. Haroche and J. M. Raimond, *Exploring the Quantum: Atoms, Cavities, and Photons* (Oxford University, 2006).
4. A. Kavokin, ed., *Microcavities*, 2nd ed., Vol. **16** of Series on Semiconductor Science and Technology (Oxford University, 2017).
5. D. N. Basov, A. Asenjo-Garcia, P. J. Schuck, X. Zhu, and A. Rubio, "Polariton panorama," Nanophotonics **10**, 549–577 (2021).
6. D. De Bernardis, P. Pilar, T. Jaako, S. De Liberato, and P. Rabl, "Breakdown of gauge invariance in ultrastrong-coupling cavity QED," Phys. Rev. A **98**, 053819 (2018).
7. C. Sánchez Muñoz, F. Nori, and S. De Liberato, "Resolution of superluminal signalling in non-perturbative cavity quantum electrodynamics," Nat. Commun. **9**, 1924 (2018).
8. O. Di Stefano, A. Settineri, V. Macrì, L. Garziano, R. Stassi, S. Savasta, and F. Nori, "Resolution of gauge ambiguities in ultrastrong-coupling cavity quantum electrodynamics," Nat. Phys. **15**, 803–808 (2019).
9. A. Stokes and A. Nazir, "Gauge ambiguities imply Jaynes-Cummings physics remains valid in ultrastrong coupling QED," Nat. Commun. **10**, 499 (2019).
10. A. F. Kockum, A. Miranowicz, S. De Liberato, S. Savasta, and F. Nori, "Ultrastrong coupling between light and matter," Nat. Rev. Phys. **1**, 19–40 (2019).
11. P. Forn-Díaz, L. Lamata, E. Rico, J. Kono, and E. Solano, "Ultrastrong coupling regimes of light-matter interaction," Rev. Mod. Phys. **91**, 025005 (2019).
12. J. Khurgin, "Excitonic radius in the cavity polariton in the regime of very strong coupling," Solid State Commun. **117**, 307–310 (2001).
13. J. B. Khurgin, "Pliable polaritons: Wannier exciton-plasmon coupling in metal-semiconductor structures," Nanophotonics **8**, 629–639 (2019).
14. H. Zhang, N. Y. Kim, Y. Yamamoto, and N. Na, "Very strong coupling in GaAs-based optical microcavities," Phys. Rev. B **87**, 115303 (2013).
15. S. Brodbeck, S. De Liberato, M. Amthor, M. Klaas, M. Kamp, L. Worschech, C. Schneider, and S. Höfling, "Experimental verification of the very strong coupling regime in a GaAs quantum well microcavity," Phys. Rev. Lett. **119**, 027401 (2017).
16. J. Levinsen, G. Li, and M. M. Parish, "Microscopic description of exciton-polaritons in microcavities," Phys. Rev. Res. **1**, 033120 (2019).
17. E. Laird, F. M. Marchetti, D. K. Efimkin, M. M. Parish, and J. Levinsen, "Rydberg exciton-polaritons in a magnetic field," Phys. Rev. B **106**, 125407 (2022).
18. E. Cortese, I. Carusotto, R. Colombelli, and S. D. Liberato, "Strong coupling of ionizing transitions," Optica **6**, 354–361 (2019).
19. E. Cortese and S. De Liberato, "Exact solution of polaritonic systems with arbitrary light and matter frequency-dependent losses," J. Chem. Phys. **156**, 084106 (2022).
20. E. Cortese, N.-L. Tran, J.-M. Manceau, A. Bousseksou, I. Carusotto, G. Biasiol, R. Colombelli, and S. De Liberato, "Excitons bound by photon exchange," Nat. Phys. **17**, 31–35 (2021).
21. S. Rajabali, E. Cortese, M. Beck, S. De Liberato, J. Faist, and G. Scalari, "Polaritonic nonlocality in light–matter interaction," Nat. Photonics **15**, 690–695 (2021).
22. A. A. Anappara, A. Tredicucci, G. Biasiol, and L. Sorba, "Electrical control of polariton coupling in intersubband microcavities," Appl. Phys. Lett. **87**, 051105 (2005).
23. T. Schwartz, J. A. Hutchison, C. Genet, and T. W. Ebbesen, "Reversible switching of ultrastrong light-molecule coupling," Phys. Rev. Lett. **106**, 196405 (2011).
24. J. Mornhinweg, M. Halbhuber, C. Ciuti, D. Bougeard, R. Huber, and C. Lange, "Tailored subcycle nonlinearities of ultrastrong light-matter coupling," Phys. Rev. Lett. **126**, 177404 (2021).
25. G. Günter, A. A. Anappara, J. Hees, A. Sell, G. Biasiol, L. Sorba, S. De Liberato, C. Ciuti, A. Tredicucci, A. Leitenstorfer, and R. Huber, "Sub-cycle switch-on of ultrastrong light–matter interaction," Nature **458**, 178–181 (2009).
26. M. Halbhuber, J. Mornhinweg, V. Zeller, C. Ciuti, D. Bougeard, R. Huber, and C. Lange, "Non-adiabatic stripping of a cavity field from electrons in the deep-strong coupling regime," Nat. Photonics **14**, 675–679 (2020).
27. S. Yu, J. Lu, V. Ginis, S. Kheifets, S. W. D. Lim, M. Qiu, T. Gu, J. Hu, and F. Capasso, "On-chip optical tweezers based on freeform optics," Optica **8**, 409–414 (2021).
28. D. Meiser and P. Meystre, "Superstrong coupling regime of cavity quantum electrodynamics," Phys. Rev. A **74**, 065801 (2006).
29. N. M. Sundaresan, Y. Liu, D. Sadri, L. J. Szöcs, D. L. Underwood, M. Malekakhlagh, H. E. Türeci, and A. A. Houck, "Beyond strong coupling in a multimode cavity," Phys. Rev. X **5**, 021035 (2015).
30. Y. Liu and A. A. Houck, "Quantum electrodynamics near a photonic bandgap," Nat. Phys. **13**, 48–52 (2017).
31. S. De Liberato, "Light-matter decoupling in the deep strong coupling regime: the breakdown of the Purcell effect," Phys. Rev. Lett. **112**, 016401 (2014).

32. A. Bayer, M. Pozimski, S. Schambeck, D. Schuh, R. Huber, D. Bougeard, and C. Lange, "Terahertz light–matter interaction beyond unity coupling strength," Nano Lett. **17**, 6340–6344 (2017).
33. X. Chen, Y.-H. Chen, J. Qin, D. Zhao, B. Ding, R. J. Blaikie, and M. Qiu, "Mode modification of plasmonic gap resonances induced by strong coupling with molecular excitons," Nano Lett. **17**, 3246–3251 (2017).
34. D. Hagenmüller, S. De Liberato, and C. Ciuti, "Ultrastrong coupling between a cavity resonator and the cyclotron transition of a two-dimensional electron gas in the case of an integer filling factor," Phys. Rev. B **81**, 235303 (2010).
35. G. Scalari, C. Maissen, D. Turcinkova, D. Hagenmuller, S. De Liberato, C. Ciuti, C. Reichl, D. Schuh, W. Wegscheider, M. Beck, and J. Faist, "Ultrastrong coupling of the cyclotron transition of a 2D electron gas to a THz metamaterial," Science **335**, 1323–1326 (2012).
36. G. Scalari, C. Maissen, D. Hagenmüller, S. De Liberato, C. Ciuti, C. Reichl, W. Wegscheider, D. Schuh, M. Beck, and J. Faist, "Ultrastrong light-matter coupling at terahertz frequencies with split ring resonators and inter-landau level transitions," J. Appl. Phys. **113**, 136510 (2013).
37. X. Li, M. Bamba, Q. Zhang, S. Fallahi, G. C. Gardner, W. Gao, M. Lou, K. Yoshioka, M. J. Manfra, and J. Kono, "Vacuum Bloch–Siegert shift in Landau polaritons with ultra-high cooperativity," Nat. Photonics **12**, 324–329 (2018).
38. W. Kohn, "Cyclotron resonance and de Haas-Van Alphen oscillations of an interacting electron gas," Phys. Rev. **123**, 1242 (1961).
39. T. Maag, A. Bayer, S. Baierl, M. Hohenleutner, T. Korn, C. Schüller, D. Schuh, D. Bougeard, C. Lange, R. Huber, M. Mootz, J. E. Sipe, S. W. Koch, and M. Kira, "Coherent cyclotron motion beyond Kohn's theorem," Nat. Phys. **12**, 119 (2016).
40. V. V. Popov, O. V. Polischuk, and M. S. Shur, "Resonant excitation of plasma oscillations in a partially gated two-dimensional electron layer," J. Appl. Phys. **98**, 033510 (2005).
41. M. Białek, M. Czapkiewicz, J. Wróbel, V. Umansky, and J. Łusakowski, "Plasmon dispersions in high electron mobility terahertz detectors," Appl. Phys. Lett. **104**, 263514 (2014).
42. G. L. Paravicini-Bagliani, G. Scalari, F. Valmorra, J. Keller, C. Maissen, M. Beck, and J. Faist, "Gate and magnetic field tunable ultrastrong coupling between a magnetoplasmon and the optical mode of an LC cavity," Phys. Rev. B **95**, 205304 (2017).
43. C. R. Gubbin, S. A. Maier, and S. De Liberato, "Real-space hopfield diagonalization of inhomogeneous dispersive media," Phys. Rev. B **94**, 205301 (2016).
44. J. J. Hopfield, "Theory of the contribution of excitons to the complex dielectric constant of crystals," Phys. Rev. **112**, 1555–1567 (1958).
45. A. A. Anappara, S. De Liberato, A. Tredicucci, C. Ciuti, G. Biasiol, L. Sorba, and F. Beltram, "Signatures of the ultrastrong light-matter coupling regime," Phys. Rev. B **79**, 201303 (2009).
46. S. De Liberato, "Virtual photons in the ground state of a dissipative system," Nat. Commun. **8**, 1465 (2017).
47. S. De Liberato, "Comment on "System-environment coupling derived by Maxwell's boundary conditions from the weak to the ultrastrong light-matter-coupling regime"," Phys. Rev. A **89**, 017801 (2014).
48. M. Bamba and T. Ogawa, "Recipe for the Hamiltonian of system-environment coupling applicable to the ultrastrong-light-matter-interaction regime," Phys. Rev. A **89**, 023817 (2014).
49. S. Franke, S. Hughes, M. K. Dezfouli, P. T. Kristensen, K. Busch, A. Knorr, and M. Richter, "Quantization of quasinormal modes for open cavities and plasmonic cavity quantum electrodynamics," Phys. Rev. Lett. **122**, 213901 (2019).
50. I. Medina, F. J. García-Vidal, A. I. Fernández-Domínguez, and J. Feist, "Few-mode field quantization of arbitrary electromagnetic spectral densities," Phys. Rev. Lett. **126**, 093601 (2021).
51. Y. Todorov, "Dipolar quantum electrodynamics of the two-dimensional electron gas," Phys. Rev. B **91**, 125409 (2015).
52. C. Maissen, G. Scalari, F. Valmorra, M. Beck, J. Faist, S. Cibella, R. Leoni, C. Reichl, C. Charpentier, and W. Wegscheider, "Ultrastrong coupling in the near field of complementary split-ring resonators," Phys. Rev. B **90**, 205309 (2014).
53. M. Załużny and W. Zietkowski, "Intersubband cavity polaritons: The role of higher photonic modes," Phys. Rev. B **80**, 245301 (2009).
54. S. Das Sarma and J. J. Quinn, "Collective excitations in semiconductor superlattices," Phys. Rev. B **25**, 7603–7618 (1982).
55. S. Rajabali, J. Enkner, E. Cortese, M. Beck, S. De Liberato, J. Faist, and G. Scalari "An engineered planar plasmonic reflector for polaritonic mode confinement," Phys. Rev. (to be published).